

35/63



CERN LIBRARIES, GENEVA



SCAN-9701200

# OXFORD UNIVERSITY

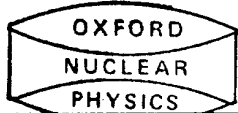
**REFERENCE ONLY  
DO NOT REMOVE**

The Physics of Charged Particle Identification:

$dE/dx$ , Cerenkov and Transition Radiation.

W.W.M. Allison and P.R.S. Wright

OUNP 35 - 83



NUCLEAR PHYSICS  
LABORATORY

Ref. No: 35/83

**The Physics of Charged Particle Identification:  
 $dE/dx$ , Cerenkov and Transition Radiation.**

**W.W.M. Allison,  
Nuclear Physics Laboratory, Oxford.**

**P.R.S. Wright,  
CERN, Geneva.**

**I. Introduction**

**II. Theory**

**II.1 General discussion**

**II.2 Cerenkov Radiation and  $dE/dx$**

**II.2.1 Simple model**

**II.2.2 Careful calculation**

**II.3 Transition Radiation and Cerenkov Radiation**

**III. Calculations for practical devices**

**III.1 Cerenkov counters**

**III.2 Transition Radiation devices**

**III.3  $dE/dx$  detectors**

**III.3.1 Theoretical spectra and their velocity dependence**

**III.3.2 Determining velocity from experimental measurements**

**III.3.3 The calibration problem**

**III.3.4 Example of performance that can be achieved**

**Appendix: The solution of practical problems for  $dE/dx$  detectors.**

## I. INTRODUCTION

The analysis of most High Energy Physics experiments requires a knowledge of the 4-momenta, ( $p, E$ ) of the secondary particles. The 3-momenta,  $p$ , are usually obtained by measuring the deflection of the trajectory of each of the particles in a magnetic field. A further measurement, be it of mass, energy or velocity, is needed to determine the fourth component of the 4-momentum,  $E$ , and fix a value for the mass  $M$ . Since  $M$  uniquely (for charged particles) identifies the internal quantum numbers, this measurement is generally referred to as "particle identification".

At low energies particle identification has traditionally been achieved by total absorption calorimetry, by time-of-flight measurement or by simple  $dE/dx$  measurements. Calorimetry becomes more difficult at higher energies, as the number of interaction lengths of absorber needed to contain the showers completely becomes large. More seriously, the energy resolution,  $\Delta E/E$ , required to distinguish different masses varies as  $E^{-2}$ , while the resolution achievable varies as  $E^{-1/2}$ . Time-of-flight measurements yield the velocity of the particles over a given distance. The time difference,  $\Delta t$ , for two particles of masses  $M_1$  and  $M_2$ , with the same momentum,  $p$ , over a distance  $L$ , is given by:

$$\Delta t = 1/2 (M_1^2 - M_2^2) Lc/p$$

Resolvable values of  $\Delta t$  are currently  $\sim 250\text{ps}$  and so, for a reasonable value of  $L$  of a few metres,  $\Delta t$  becomes unmeasurably small for  $p > 1 \text{ GeV}/c$ . In the non-relativistic range energy loss ( $dE/dx$ ) is proportional to  $1/\beta^2$  ( $\beta c$  is the particle velocity). This gives a large difference in signal amplitude for different masses. As  $\beta$  approaches one however, this simple discrimination is no longer possible.

For these reasons other methods of particle identification have been developed for the relativistic range. They are based on the following physical effects:

- a) Cerenkov Radiation: If a charged particle moves through a medium faster than the phase velocity of light in that medium, it will emit radiation at an angle determined by its velocity and the refractive index of the medium. Either the presence/absence of this radiation (in threshold Cerenkov counters), or a direct measurement of the Cerenkov angle (Differential or Ring-Image Cerenkov counters) can be used to give information on the particle velocity.

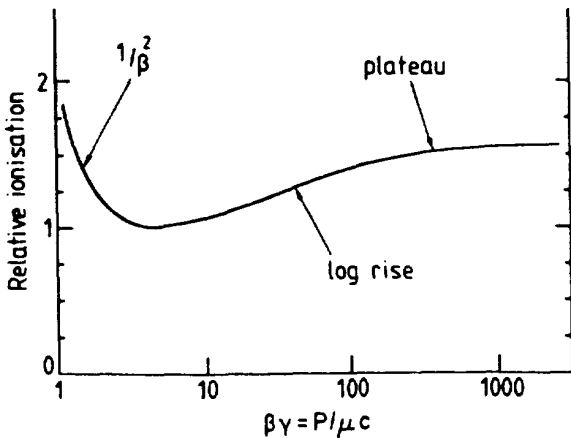


Fig.1. The dependence of ionisation in a gas on  $\beta\gamma$ .

- b) Energy loss ( $dE/dx$ ): The rate of energy loss for a relativistic particle is a weak function of the  $\beta\gamma$  of the particle ( $\beta\gamma = p/Mc = \frac{v}{c} [1 - \frac{v^2}{c^2}]^{-1/2}$ ). This dependence is shown in fig.1. In the non-relativistic region ( $\beta\gamma < 4$ ) the rate of energy loss falls to a minimum as  $1/\beta^2$ . Above  $\beta\gamma \approx 4$  the rate of energy loss rises again as  $\log(\beta\gamma)$ ; this is the so-called relativistic rise. At  $\beta\gamma$  of a few hundred the rate of energy loss saturates (the "Fermi plateau"). In solids and liquids the plateau is only a few percent above the minimum; in high-Z noble gases at atmospheric pressure it reaches 50-70%. An accurate measurement of the energy loss in the relativistic rise region provides a measurement of  $\beta\gamma$ , and hence of  $M$ .
- c) Transition Radiation: When a highly relativistic particle ( $\beta\gamma \gtrsim 500$ ) crosses the boundary between two dielectric media, x-ray photons are emitted. The energy of these photons is a function of  $\beta\gamma$ . Hence by measuring the transition radiation the mass of the particle may be obtained.

The above phenomena are intimately related, all depending on the dielectric properties of the medium and the velocity of the charged particle. Their treatment in standard texts is often cursor, disjointed, and without some of the details needed to design and predict the performance of a practical device. In Section II we discuss the theoretical ideas that link these three phenomena together. Section III demonstrates how these theoretical ideas may be applied to practical devices. Finally, in an appendix we discuss some particular practical

problems and solutions for  $dE/dx$  devices.

An elementary introduction to Cerenkov radiation is given in the Nobel Prize lectures (Cerenkov 1958) and a full discussion is given by Jelley (1958) and Ter-Mikaelian (1972). The latter also treat the theory of Transition Radiation. Useful treatments are also to be found in Jackson (1962) and Landau & Lifshitz (1960). The theory of X-ray transition radiation is described by Garibyan (1957). The theory of  $dE/dx$  is described fully and with references in Allison & Cobb (1980). Some elements of the development are to be found in Jackson (1975), Fano (1963) and Landau & Lifshitz (1960). The details of how it might be used for particle identification were first worked out by Alikhanov (1956).

## II. THEORY

### II.1 General Discussion

Any device that is to detect a particle must interact with it in some way. If the particle is to pass through essentially undeviated, this interaction must be a soft electromagnetic one. Let us consider a particle of mass  $M$  and velocity  $\underline{v}$ , which interacts with the medium of the detector via a photon of energy  $\hbar\omega$  and momentum  $\hbar\underline{k}$ , as shown in fig.2. Conservation of energy and momentum require:

$$\hbar\omega (1 - \hbar\omega/2\gamma Mc^2) = \hbar \underline{k} \cdot \underline{v} - \hbar k^2/2\gamma M$$

With the restriction to soft collisions,  $\hbar\omega \ll \gamma Mc^2$  and  $\hbar k \ll v\gamma M$ , this reduces to:

$$\omega = \underline{v} \cdot \underline{k} \quad (1)$$

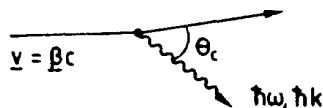


Fig.2. Photon emission in a medium.

The behaviour of a photon in a medium is described by the dispersion relation

$$\omega^2 - k^2 c^2/\epsilon = 0 \quad (2)$$

where  $\epsilon$  is the relative electric permittivity or dielectric constant.

Eliminating  $\omega$  and  $k$  between eqns.(1) and (2) gives:

$$\sqrt{\epsilon} \frac{v}{c} \cos\theta_c = 1 \quad (3)$$

where  $\theta_c$  is the angle between  $v$  and  $k$ . This shows that, if  $\frac{v}{c}$  is greater than unity, a real angle  $\theta_c$  exists for which free photons can be emitted (or absorbed). This is known as the Cerenkov angle and the free photon flux as Cerenkov radiation. The velocity at which  $v$  is equal to  $c/\sqrt{\epsilon}$  is called the Cerenkov threshold. At lower velocities  $\cos\theta_c$  is greater than unity, and free photons are not emitted in continuous media. In discontinuous media diffraction causes free photon emission even below the Cerenkov threshold (see II.3).

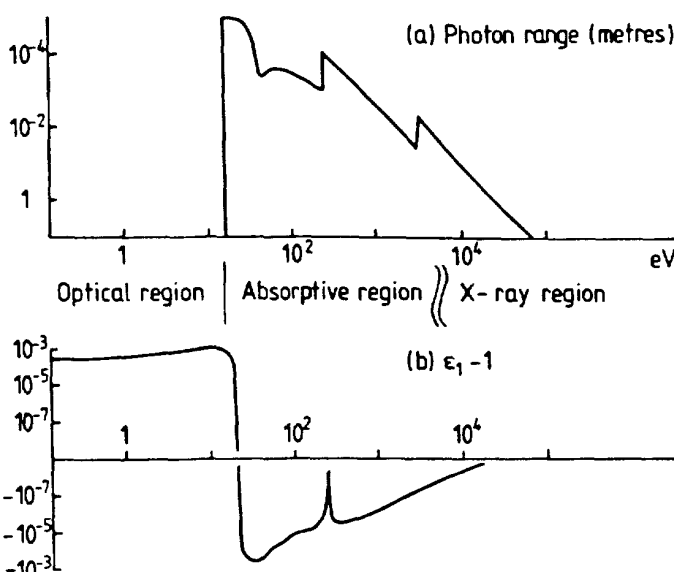


Fig.3. The dependence of  $\epsilon$  for argon at normal density on photon energy,  
a) imaginary part expressed as a range and  
b) real part - 1 on a split log scale.

So far it has been assumed that  $\epsilon$  is real. In practice this is only true below the ionisation threshold of the medium. Fig.3 shows  $\epsilon$  as a function of frequency for argon gas as an example. There are three important frequency ranges:

- The Optical region. For frequencies below the absorption region the medium is transparent,  $\epsilon$  is real and greater than one, and Cerenkov radiation is emitted by particles with velocity above the threshold (which is always less than  $c$ ). The emission of subthreshold Cerenkov radiation by discontinuities in the medium is called Optical Transition Radiation which is not important for

- particle identification.
- b) The absorption region.  $\epsilon$  is complex and the range of photons is short. Absorption of the virtual photons constituting the field of a charged particle gives rise to the ionisation of the material that is measured in  $dE/dx$  detectors.
  - c) The X-ray region. The residual absorptive part of  $\epsilon$  still causes a small contribution to be made to the tail of the  $dE/dx$  distribution but at frequencies some 30% above its K-edge the medium may be treated as being nearly transparent. There  $\epsilon$  is less than one, however, and the Cerenkov threshold is greater than c. Nevertheless, the emission of sub-threshold Cerenkov radiation in the presence of discontinuities in the medium may still occur; this is known as X-ray Transition Radiation, and is exploited by Transition Radiation detectors.

In the following sections we derive formulae for the magnitude of the energy-loss signal, the flux of Cerenkov radiation, as well as the Transition Radiation effect. This is much simpler than is often supposed and in particular Quantum Electrodynamics is not needed at any stage. The formalism of Maxwell's Equations with semi-classical quantisation, as in Planck's description of black-body radiation, is all that is necessary, apart from the knowledge of  $\epsilon$  for the media concerned.

## II.2 Cerenkov radiation and $dE/dx$

### II.2.1 Simple model

To discuss the relationship between Cerenkov radiation and  $dE/dx$  let us consider the field seen by an observer at a point  $(x,y)$  due to a particle moving along the x-axis. To simplify the picture we ignore the z-dimension - the effect of this is to give exponentials in place of Bessel functions which eases the manipulation without altering any principles of physics.

Such an observer sees an electromagnetic pulse as the particle goes by. This pulse is made up of a broad spectrum of frequency components and travels in the x direction with velocity v without dispersion. These conditions require that the phase velocity in the x direction for each Fourier component satisfies equation (1). This means that the components of the field are components of a static field as seen by an

observer comoving with the particle. We therefore have  $k_x = \frac{\omega}{v}$  and  $k_x^2 + k_y^2 = \frac{\omega^2 \epsilon}{c^2}$  from equation (2), giving  $k_y = \frac{\omega}{v} (\frac{v^2 \epsilon}{c^2} - 1)^{1/2}$ . Let us

call the phase velocity of light in the medium  $u(\omega) = c/\sqrt{\epsilon}$ . Then this becomes:

$$k_y = \frac{\omega}{v} \left( \frac{v^2}{u^2} - 1 \right)^{1/2}$$

There are two situations to which this formula can be applied:

a) v greater than u. Then  $k_y$  is real and the component of frequency  $\omega$  represents a real travelling wave at an angle  $\cos^{-1}(u/v)$ . This is the case of Cerenkov Radiation.

b) v less than u.  $k_y$  is now purely imaginary and the component of frequency  $\omega$  propagates as an evanescent wave in the transverse direction (just like the evanescent wave encountered in the phenomenon of total internal reflection):

$$\exp i(k_r \cdot r - \omega t) = \exp i \frac{\omega}{v} (x - vt) \exp - y/y_0$$

where the range  $y_0$  is given by

$$y_0 = \frac{v}{\omega} (1 - v^2/u^2)^{-1/2}$$

Re-expressed in terms of the dimensionless variable,  $\beta' = v/u$ ,  $\gamma' = (1-\beta'^2)^{-1/2}$  and  $\bar{x} = u/\omega$ , the free wavelength over  $2\pi$ , the range becomes

$$y_0 = \bar{x} \beta' \gamma' \quad (4)$$

This shows that the range of the field expands linearly with the dimensionless scaled variables  $\beta' \gamma'$  as the Cerenkov threshold is approached. This expansion, often referred to as 'the relativistic expansion', depends only on the wave nature of the field and is responsible for the 'relativistic rise' of the ionisation cross section.

The velocity of light in vacuum,  $c$ , only enters the problem through the kinematics of the particle itself - which is strictly irrelevant to the soft electromagnetic field of the particle in a medium. However in practice we are interested in the dependence of the field on the dimensionless scaled variables appropriate to the vacuum,  $\beta = v/c$  and  $\gamma = (1-\beta^2)^{-1/2}$ . Then the clear formula (4) appears more complicated:

$$y_0 = \bar{x} \beta \left( \frac{1}{\gamma^2} + (1-\epsilon) \beta^2 \right)^{-1/2} \quad (5)$$

The complexity however has only arisen from the change of variables.

In considering equation (5) we distinguish two cases of interest depending on whether  $\epsilon$  is greater than unity or not:

a)  $\epsilon > 1$ . As shown in figure 3 this implies that the frequency is in the Optical region below the ionisation threshold. At increasing values of velocity the range increases until at  $\beta' = 1$  (and  $\gamma' = \infty$ ), the range becomes infinite and we have a Cerenkov field.

b)  $\epsilon < 1$ . Here  $\omega$  is above ionisation threshold (the absorption and x-ray regions). The range increases with increasing values of velocity as before but reaches an upper bound when  $\beta' = c/u$ . This plateau is given by equation (5) for ( $\beta = 1$ ,  $\gamma = \infty$ ) by

$$y_0 = \pi (1-\epsilon)^{-1/2}$$

The plateau, which gives a corresponding saturation in the relativistic rise of the ionisation cross section, starts to set in at velocities for which the two terms in the denominator of equation (5) are equal i.e.

$$\beta\gamma \sim (1-\epsilon)^{-1/2}$$

For different frequencies the plateau becomes important for different values of  $\beta\gamma$  depending on  $\epsilon(\omega)$ . Nevertheless in any kind of sum over frequencies the same general effect is apparent. The  $dE/dx$  dependence shown in fig.1 is an example. At the highest values of  $\beta\gamma$  the energy loss saturates ("the density effect"). This plateau sets an upper bound to the range of  $\beta\gamma$  over which  $dE/dx$  may be used to measure velocity effectively. Since  $(1-\epsilon)$  scales with the density the onset of saturation varies as  $\rho^{-1/2}$ . For velocity discrimination at high values of  $\beta\gamma$ ,  $\epsilon$  must be close to unity and gases must be used.

There is a corresponding limit beyond which the Cerenkov field becomes asymptotic as a function of  $\beta\gamma$ . The Cerenkov angle is within a value  $\delta\theta$  of its asymptotic value for values of  $\beta\gamma$  given by

$$\beta\gamma \sim (\epsilon-1)^{-1/4} (\delta\theta)^{-1/2}$$

and the flux is within 90% of its asymptotic value for  $\beta\gamma$  greater than

$$\beta\gamma \sim 3(\epsilon-1)^{-1/2}$$

Taking nitrogen at normal density as an example ( $\epsilon-1=594 \times 10^{-6}$ ), and  $\delta\theta=10$  mrad the two  $\beta\gamma$  values come out to be 64 and 123. The  $dE/dx$  signal also saturates around  $\beta\gamma=100$ . The need to work with low density gases is therefore evident in both Cerenkov and  $dE/dx$  techniques and the reason is essentially the same.

### III.2.2 Careful calculation

Since it is a form of energy loss, Cerenkov Radiation should appear in a natural way from a rigorous calculation of  $dE/dx$ . Such a calculation may be made using the Photo Absorption Ionisation Model for any mixture of gases whose photo-absorption spectra are available. These calculations have been described in detail elsewhere (Allison & Cobb (1980)). A FORTRAN program and data files are available for further calculations. Here we describe the physics of the five main steps involved in the derivation of the energy-loss differential cross section.

#### Step 1

This is a conventional problem in Classical Electrodynamics. We solve Maxwell's Equations in a medium ( $D=\epsilon\epsilon_0 E$ ,  $\mu=1$ ) due to a charge density,  $\rho=e\delta^3(r-\beta ct)$ , and current density,  $j=\beta c\rho$ , which together describe a charge moving with velocity,  $\beta c$ . Working in SI units and the Coulomb Gauge one obtains

$$\phi(\underline{k}, \omega) = \frac{e}{2\pi\epsilon\epsilon_0 k^2} \delta(\omega - \underline{k}\cdot\underline{\beta c})$$

$$A(\underline{k}, \omega) = \frac{e}{2\pi\epsilon\epsilon_0 c^2} \frac{(\omega\underline{k}/k^2 - \underline{\beta c})}{(\epsilon\omega^2/c^2 - k^2)} \delta(\omega - \underline{k}\cdot\underline{\beta c})$$

with

$$\underline{E}(r, t) = \frac{1}{(2\pi)^2} \iint [i\omega A(\underline{k}, \omega) - ik\phi(\underline{k}, \omega)]$$

$$\times \exp i(\underline{k}\cdot\underline{r} - \omega t) d^3k d\omega$$

#### Step 2

The energy loss is due to the component of this electric field in the direction  $\beta$  doing work on the particle itself at the point  $r=\beta ct$ :

$$\langle dE/dx \rangle = \frac{e}{\beta} \underline{E}(\beta ct, t) \cdot \underline{\beta}$$

#### Step 3

This energy loss, which is expressed as an integral over Fourier components, is not a smooth rate of energy loss but needs to be re-interpreted as in semiclassical radiation theory as a probability of

energy transfers,  $E = \hbar\omega$ . Thus

$$\langle dE/dx \rangle = - \int_0^\infty d\omega \int_{\omega/v}^\infty dk N E \frac{d^2\sigma}{dE dp} \hbar^2 d\omega dk$$

where  $N$  is the electron density and  $\frac{d^2\sigma}{dE dp}$  is the double differential cross section per electron. Doing the implied algebra we get

$$\frac{d^2\sigma}{dE dp} = \frac{e^2}{4\pi\epsilon_0} \frac{2}{N\beta^2\pi\hbar^2} \left[ p(\beta^2 - \frac{E^2}{p^2c^2}) m(\frac{1}{\epsilon E^2 - p^2c^2}) - \frac{1}{pc^2} m(\frac{1}{\epsilon}) \right]$$

This formula already shows the  $1/\beta^2$  factor which dominates the rate of energy loss at non relativistic velocities.

#### Step 4

The only unknown parameter in this formula is  $\epsilon$ . It is a complex function ( $\epsilon = \epsilon_1 + i\epsilon_2$ ) of  $k$  and  $\omega$ , and is essentially the structure function of the medium. A sufficiently reliable model (Allison & Cobb 1980) for  $\epsilon$  may be derived from

- detailed photoabsorption spectra and their sum rules giving  $\epsilon_2$  for on mass-shell photons ( $\omega = kc$ ), see Berkowitz (1979),
- the Kramers Kronig relation giving  $\epsilon_1$  in terms of  $\epsilon_2$ ,
- the dipole approximation which tells us that for small  $k$   $\epsilon(k, \omega)$  is independent of  $k$  at fixed  $\omega$ ,
- constituent scattering from quasi-free electrons and the Bethe sum rule which together give values for  $\epsilon$  in the large  $k$  off-mass-shell region.

#### Step 5

With this model it is possible to integrate the cross section over momentum transfer analytically. The differential cross section per electron per unit energy loss is:

$$\begin{aligned} \frac{d\sigma}{dE} &= \frac{\alpha}{\beta^2\pi} \frac{\sigma_Y(E)}{E Z} \ln[(1-\beta^2\epsilon_1)^2 + \beta^4\epsilon_2^2]^{-1/2} + \frac{\alpha}{\beta^2\pi} \frac{1}{Nhc} \left( \beta^2 - \frac{\epsilon_1}{|\epsilon|^2} \right) \Theta \\ &\quad + \frac{\alpha}{\beta^2\pi} \frac{\sigma_Y(E)}{E Z} \ln \left( \frac{2mc^2\beta^2}{E} \right) + \frac{\alpha}{\beta^2\pi} \frac{1}{E^2} \int_0^E \frac{\sigma_Y(E')}{Z} dE' \end{aligned} \quad (6)$$

where  $\alpha = e^2 / 4\pi \epsilon_0 c$  is the fine structure constant,  $\epsilon_1$  and  $\epsilon_2$  are the real and imaginary parts of the usual on-mass-shell dielectric constant and  $\theta$  is the phase of the complex expression  $1 - \epsilon_1 \beta^2 + i \epsilon_2 \beta^2$ .  $\sigma_\gamma$  is the atomic photo-absorption cross section of the gas.

In the first term, ignoring  $\epsilon_2$ , we recognise a factor  $\ln(1 - \beta^2 \epsilon_1)^{-1}$  or  $\ln \gamma^2$  in the notation of our simplified discussion. This is responsible for the relativistic rise of the energy-loss cross section and its saturation as already discussed. In the Optical region  $\sigma_\gamma$  vanishes and only the second term contributes. This describes energy loss by Cerenkov Radiation. In the absence of  $\epsilon_2$  the phase  $\theta$  jumps from zero below threshold to  $\pi$  above. Multiplying by  $N_h$  this term gives the flux of Cerenkov photons per unit path length

$$\frac{dn}{d\omega} = \frac{\alpha}{c} \left( 1 - \frac{1}{\beta^2 \epsilon} \right). \quad (7)$$

However when  $\epsilon_2$  and  $\sigma_\gamma$  do not vanish, the separate interpretation of this term in the cross section dissolves and it may even be negative. The last term in equation (6) comes from the constituent scattering from electrons. It is a Rutherford scattering term, shows no relativistic behaviour and, being the sole non-vanishing term for energy transfers  $E$  in the far X-ray region, describes  $\delta$ -ray production. In general it is small and its nuisance value in  $dE/dx$  measurements is often over-stated.

### II.3 Transition Radiation and Cerenkov Radiation

When a fast charged particle passes through a thin film of material, the wavefront of the Cerenkov Radiation, BC, shown in figure 4 is restricted in width. It follows that there is broadening of the

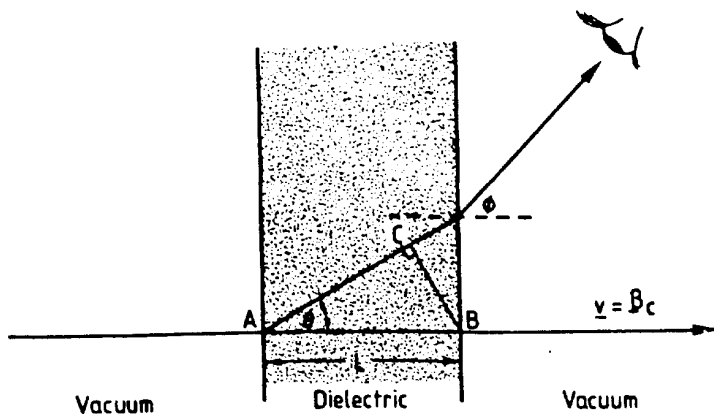


Fig.4. The emission of Cerenkov or Transition Radiation in a thin slab.

Cerenkov angle due to diffraction. This Cerenkov radiation field may be represented in one of two ways:

- a) As the sum of many wavelets whose sources are distributed along the path AB. This is the conventional Cerenkov or "differential" representation of the field.
- b) As the integral of this field due to sources at points A and B subtracted from one another. This field emitted from A and B with opposite sign is the Transition Radiation or "integral" representation of the field.

Using this integral transformation we now derive a formula for the Transition Radiation emitted from a foil starting from equation (7) for the Cerenkov flux. Since the radiation is emitted at an angle given by equation (3) we may rewrite the differential flux as

$$\frac{d^2n}{dw d\Omega} = \frac{\alpha}{2\pi c} \sin^2\theta \delta(\cos\theta - \frac{1}{\beta/\epsilon}) L$$

For L, the track length in the dielectric, small, the  $\delta$ -function should be replaced by the single slit Fraunhofer diffraction function thus

$$\delta(\cos\theta - \frac{1}{\beta/\epsilon}) + \frac{L}{\lambda} \frac{\sin^2(\Phi/2)}{(\Phi/2)^2}$$

where  $\lambda$  is the wavelength in the film and  $\Phi(\theta)$  is the phase difference between wavelets emitted from the two ends of the track in the foil, A and B:

$$\Phi(\theta) = \frac{2\pi L}{\lambda} (\cos\theta - \frac{1}{\beta/\epsilon})$$

Since L is small, the broadening of the Cerenkov angle due to diffraction can be significant. Indeed it can be large enough that radiation is observed even when the Cerenkov angle itself is unphysical. For  $\omega$  in the optical region this gives rise to Optical Transition Radiation at wide angles and at modest velocities, that is for values of  $\beta$  below Cerenkov threshold. This case is not technically important although historically it was the first to be described. The important case is the emission of Transition Radiation in the X-ray region for very large values of  $\gamma$  and at very small angles of order  $1/\gamma$ . Then  $\epsilon$  is very close to unity and may be approximated as

$$\epsilon = 1 - \frac{\omega_p^2}{\omega^2}$$

where  $\omega_p$  is the plasma frequency,  $(Ne^2/\epsilon_0 m)^{1/2}$ ,  $N$  being the electron density in the film<sup>t</sup>.

We now derive the formula for the flux of X-ray Transition Radiation from such a foil. Replacing the  $\delta$  function and substituting for  $\lambda=2\pi c/\omega/\epsilon$ , we have

$$\frac{d^2n}{d\omega d\Omega} = \frac{\alpha/\epsilon}{\pi^2 \omega} \sin^2 \theta \frac{\sin^2 [\frac{\omega L}{2c} (\sqrt{\epsilon} \cos \theta - 1/\beta)]}{(\sqrt{\epsilon} \cos \theta - 1/\beta)^2}$$

However, referring to fig.4, we see that the radiation is observed, not in the medium, but in vacuum. Since  $\sin \phi = \sqrt{\epsilon} \sin \theta$ , we have

$$\frac{d^2n}{d\omega d\Omega} = \frac{\alpha}{\pi^2 \omega} \sin^2 \phi \frac{\sin^2 [\frac{\omega L}{2c} (\sqrt{\epsilon - \sin^2 \phi} - 1/\beta)]}{(\sqrt{\epsilon - \sin^2 \phi} - 1/\beta)^2}$$

where, since  $\epsilon$  is near 1, we have ignored simple factors of  $\epsilon$ , the effect of reflection and the change in solid angle  $d\Omega$ . However the above formula contains a serious error. It is not consistent with the application of the superposition principle to the film as a radiator. The net effect of the film as a radiator must be seen as the replacement of a slice of vacuum by a slice of dielectric. There is therefore a contribution describing the absence of the vacuum field from the slice. Its amplitude is of the same form (with  $\epsilon=1$ ) but opposite phase. The  $\sin^2$  factor in the numerator describing the dependence on the phase difference  $\phi$  is common. The correct formula is therefore

$$\frac{d^2n}{d\omega d\Omega} = \frac{\alpha}{\pi^2 \omega} \sin^2 \phi \sin^2 [\frac{\omega L}{2c} (\sqrt{\epsilon - \sin^2 \phi} - 1/\beta)] \times \\ \left( \frac{1}{\sqrt{\epsilon - \sin^2 \phi} - \frac{1}{\beta}} - \frac{1}{\cos \phi - \frac{1}{\beta}} \right)^2$$

The pole of the first term, representing the Cerenkov field in the medium, is dominant in Optical Transition Radiation. The pole of the

---

<sup>t</sup> A handy formula for the plasma frequency is given by

$\hbar \omega_p = 29 \left( \frac{\rho}{1000} Z/A \right)^{1/2} \text{ev}$ , where  $\rho$  is the density in  $\text{kg m}^{-3}$ .

second term, representing the Cerenkov field in vacuum, is dominant in X-ray Transition Radiation at small angle  $\phi$  and  $\beta \sim 1$ . This pole gives X-ray Transition Radiation its unique advantage that, provided the foil is held in vacuum, this term grows ever larger as the limit  $\beta=1$  is approached. For small angles and  $\beta \sim 1$  we get the simplified result

$$\frac{d^2n}{d\omega d\Omega} = \frac{\alpha}{\pi^2 \omega} \phi^2 \cdot 4 \sin^2 \left[ \frac{\omega L}{4c} \left( \frac{\omega_p^2}{\omega^2} + \phi^2 + 1/\gamma^2 \right) \right] \times \left( \frac{1}{1/\gamma^2 + \omega_p^2/\omega^2 + \phi^2} - \frac{1}{1/\gamma^2 + \phi^2} \right)^2 \quad (8)$$

This is the usual formula for the X-ray Transition Radiation from a thin film. It is the most convenient one to work with for practical calculations.

Equation (8) represents the interference between two equal and opposite amplitudes with relative phase given by the argument of the  $\sin^2$  factor. In the absence of this interference effect the flux from each interface separately would be

$$\frac{d^2n}{d\omega d\Omega} = \frac{\alpha \phi^2}{\pi^2 \omega} \left( \frac{1}{1/\gamma^2 + \omega_p^2/\omega^2 + \phi^2} - \frac{1}{1/\gamma^2 + \phi^2} \right)^2$$

This may be integrated over the solid angle,  $d\Omega = 2\pi\phi d\phi$ , to give

$$\begin{aligned} \frac{dn}{d\omega} &= \frac{2\alpha}{\pi\omega} \left[ \left( \frac{1}{2} + \frac{\omega^2}{\gamma^2 \omega_p^2} \right) \ln \left( 1 + \frac{\gamma^2 \omega_p^2}{\omega^2} \right) - 1 \right] \\ &\approx \frac{2\alpha}{\pi\omega} \ln (\gamma \omega_p / \omega), \text{ if } \omega \ll \gamma \omega_p \end{aligned}$$

which in turn may be integrated to give a total energy flux  $\frac{\alpha}{3} \gamma h \omega_p$ , a typical photon energy of order  $1/4 \gamma h \omega_p$  and about  $\alpha$  photons per interface. The  $\gamma$  dependence of the yield is seen to come primarily from the hardening of the spectrum rather than an increase in the flux.

These latter results are somewhat academic, however, (though often quoted) since the interference term in equation (8) cannot be ignored in practice. Indeed because of this term the energy flux  $S$ , instead of increasing linearly with  $\gamma$ , saturates. This is called the Formation Zone Effect. We define a "formation zone"  $Z$ :

$$z = \frac{\lambda}{\pi} \left( \frac{1}{\gamma^2} + \frac{\omega_p^2}{\omega^2} + \phi^2 \right)^{-1}$$

Then the L dependent modulation factor in equation (8) becomes simply:  $4\sin^2(L/z)$ . Negative interference is therefore general when  $L \ll z$ . Since for a particular  $\gamma$  the significant values of  $\omega$  are of order  $\gamma\omega_p$  and  $\phi$  is of order  $1/\gamma$ ,

$$z \sim \frac{\lambda\gamma^2}{3\pi}$$

Thus the Transition Radiation flux instead of increasing linearly with  $\gamma$  will saturate around  $\gamma \sim (3\pi L/\lambda)^{-1/2}$ . Alternatively this formula indicates the minimum foil thickness required to avoid saturation at a given value of  $\gamma$ .

### III. CALCULATIONS FOR PRACTICAL DEVICES

#### III.1 Cerenkov counters

Cerenkov counters measure the particle velocity either by simply recording the flux of radiation as given by equation (7) (threshold counters) or by measuring its characteristic angle with respect to the line of flight of the particle, as given by equation (3) (Differential counters and Ring Imaging Cerenkov counters). They have been reviewed by Litt & Meunier (1973). Recent advances are described by Ypsilantis 1981, and examples given by Glass (1983) and Davenport (1983). The velocity range, the frequency range  $\Delta\omega$  and the radiator length  $L$  are crucial to the number of photons emitted:

$$n = \frac{a}{c} L \Delta\omega \left(1 + \beta_t \gamma_t\right)^{-1} \left[1 - \left(\frac{\beta_t \gamma_t}{\beta \gamma}\right)^2\right]$$

where  $\beta_t \gamma_t$  is the  $\beta \gamma$  value at threshold. The first bracket indicates that the length  $L$  required rises almost linearly with the desired value of  $\beta_t \gamma_t$  - this follows directly from the need to get the appropriate value of  $\epsilon$ . The range of  $\beta \gamma$  in which the Cerenkov flux rises from threshold to 90% of its asymptotic value is given by:

$$\beta_t \gamma_t < \beta \gamma < 3\beta_t \gamma_t \text{ or } (\epsilon-1)^{-1/2} < \beta \gamma < 3(\epsilon-1)^{1/2}.$$

The threshold is determined by the value of  $\epsilon$  for the radiator. It is convenient, where possible, to choose a gas at atmospheric pressure as other pressures necessitate thick windows that introduce unwanted scattering and secondary interactions. Some useful values are given in the table for gases at 1 atm and 0°C:

	$(\epsilon-1) \cdot 10^6$	$\beta_t \gamma_t$
Helium	72	118
Neon	134	86
Hydrogen	264	62
Argon	562	42
Nitrogen	594	41
Methane	888	33
Carbon dioxide	902	33
n-Pentane	3422	17

For values of  $\epsilon$  closer to unity, low-density gas radiators employ sub-atmospheric pressure or high temperature. For instance a large multicell Cerenkov with high threshold employing helium at normal pressure and 300 degrees centigrade is operational as part of the European Hybrid Spectrometer at CERN (Ladron de Guevara 1983). For lower thresholds a special material, "silica aerogel", is available. This is a substance which may be prepared with refractive index in the range 1.01-1.05 (see Poelz and Riethmuller 1982 and refs quoted there).

The number of photons actually detected depends on the product of the number generated (according to equation (7)), the transmission of the optical components (including windows and the reflection coefficient of mirrors) and the quantum efficiency of the final detecting elements. The latter may be photomultipliers or a gas in a proportional counter with very low ionisation threshold such as TMAE (Ypsilantis 1981). The product of these factors determines an effective bandwidth since at long wavelengths the quantum efficiency of the detector falls to zero while at short wavelengths the transmission of the optical system cuts off. Although there is a considerable advantage in extending the sensitivity into the ultraviolet, the dispersion of the refractive index in this region smears the threshold, the Cerenkov angle and the velocity resolution. Noble gases have least dispersion and are usually chosen where the ultraviolet region is to be used. Care has to be taken to avoid radiators that scintillate. In experiments with a number of secondary particles the problem of identifying which photons belong to which particles has to be solved. On the other hand in Transition Radiation or  $dE/dx$  detectors the signals are usually superimposed on the particle trajectory.

### III.2 Transition Radiation devices

Equation (8) gives the flux of X-ray Transition Radiation from a single foil in vacuum. For a foil in a gas the denominator of the last term needs an additional  $+\omega_p^2/\omega^2$ , where  $\omega_p$  is the plasma frequency of the gas. The flux is so low that many such foils must be used to make an efficient radiator. However the observed flux is not  $N$  times the single foil flux, for a number of reasons:

First there is coherence between foils. For complete coherence we would have

$$\frac{dn_N}{d\omega} = \frac{\sin^2[N(\frac{\Phi + \Phi_G}{2})]}{\frac{(\Phi + \Phi_G)^2}{2}} \cdot \frac{dn_1}{d\omega}$$

where  $\Phi(\phi)$  is the phase difference across one foil introduced in II.3 and  $\Phi_G(\phi)$  is the corresponding phase difference across the gap between foils. If each foil is typically a formation zone thick, so as not to suppress  $\frac{dn_1}{d\omega}$ , the radiation from one foil,  $\Phi(\phi)$  is not small. It follows that  $\Phi_G$  must not be small either and the foil separation must be greater than or equal to the formation zone in the gas otherwise there will be destructive interference between successive foils.

At low frequencies the effect of self absorption of the X-rays by the foils is also important. The general case is given by

$$\frac{dn_N}{d\omega} = \frac{1 + \exp(-N\sigma) - 2 \exp(-N\sigma/2) \cos N(\Phi + \Phi_G)}{1 + \exp(-\sigma) - 2 \exp(-\sigma/2) \cos (\Phi + \Phi_G)} \times \frac{dn_1}{d\omega}$$

where  $\sigma = \mu_d + \mu_G d_G$ , the combined attenuation of a foil and a gap. These interference effects have been demonstrated experimentally for a small number of foils (Fabjan 1975) and have been analysed theoretically (Artru 1975). For a large number of foils such as is appropriate for an optimised detector the effect of multiple scattering can be important in reducing coherence over the whole stack. This happens when

$$\phi_{ms} = \frac{15}{\gamma M(\text{MeV}/c^2)} \cdot \left( \frac{l}{l_{rad}} \right)^{1/2}$$

is of the same order as the peak angle  $\phi \sim 1/\gamma$ . The effect is therefore independent of  $\gamma$ , occurs at  $l/l_{rad} = 10^{-3}$  for electrons and is negligible

for other particles. There are no accepted handy formulae for including the effect of multiple scattering.

The most thorough detector optimisation has been described by the Willis group (Cobb 1977), which ignored multiple scattering. The flux of photons that they observed was some 30% less than expected. It is not known whether this was due to multiple scattering or mechanical tolerances. We note that their stack of 500 50 $\mu\text{m}$  lithium foils represents  $\ell/\ell_{\text{rad}} = 16 \times 10^{-3}$ . Many practical radiators consist not of films, but of random fibres or foam (Bauche 1982). The theory of such radiators (Garibyan 1975) employing a spread of radiator elements described by a gaussian distribution has been confirmed experimentally (Fabjan 1977). A radiator incorporating 20 carbon-fibre stacks forms part of the European Hybrid Spectrometer (EHS) at CERN and is in use for experiments (Commichau 1980, Struczinski 1983). To summarise although there are effects that reduce its importance, in practice the effect of interfoil coherence may not be ignored.

The optimum choice of radiator thickness is a compromise between attenuation and formation zone suppression. The best material has high electron density (according to section II.3 the energy flux scales with  $\omega_p^w$ ) and low Z (for low X ray attenuation). The table gives a list of materials that have been or might be used.

Material	Form	Transition Radiators			
		$\omega_p^w$ (eV)	Z	K-edge (eV)	Comment
Deuterium	Foam	7.8	1	14	
Lithium	Foil	14	3	55	Cobb 77
Lithium hydride		19	3	55	
Beryllium	Foil	27	4	110	
Boron		31	5	190	
$\text{B}_4\text{C}$		32	6	280	
C	Fibres	28	6	280	Commichau 80/Bauche 82
Mylar ( $\text{C}_5\text{H}_4\text{O}_2$ )	Foil	24	8	530	Many tests
Polyethylene ( $\text{CH}_2$ )		19	6	280	

Interspersed with sections of radiator are the Transition Radiation photon detectors. To have a high quantum efficiency for a modest thickness they must contain an active absorber of high Z. To date

Xenon-filled proportional chambers have been used for real devices, although many tests have used argon or krypton which are significantly less efficient. In a sequence of radiator stacks and gas filled chambers it is necessary to take into account absorption by materials in gas gaps and windows as well as the flux not absorbed by one detector which may reach the next. For this reason optimised stacks usually include a thicker radiator at the front.

The photons are emitted at an angle of order  $1/\gamma$  with respect to the parent particle. It is not therefore usually considered practical to resolve the proportional chamber signal due to the Transition Radiation from the signal due to the  $dE/dx$  of the particle itself passing through the detector gas. It follows that signals from a Transition Radiation detector are generally the sum of  $dE/dx$  and Transition Radiation. There are two points to make. First, the relativistic rise of  $dE/dx$ , particularly pronounced in Xenon, often provides a helpful contribution in addition to the Transition Radiation. The effect may be assessed in tests by removing the radiators. Second, the broad spectra both of  $dE/dx$  and of Transition Radiation imply that a number of measurements is required. Typically between 2 (Cobb 1977) and 20 (Commichau 1980) measurements are used. Discrimination is achieved by taking the mean signal and comparing it with model distributions based on the analysis of known tracks. Fig.5 shows the  $\gamma$  dependence of the mean and FWHM of

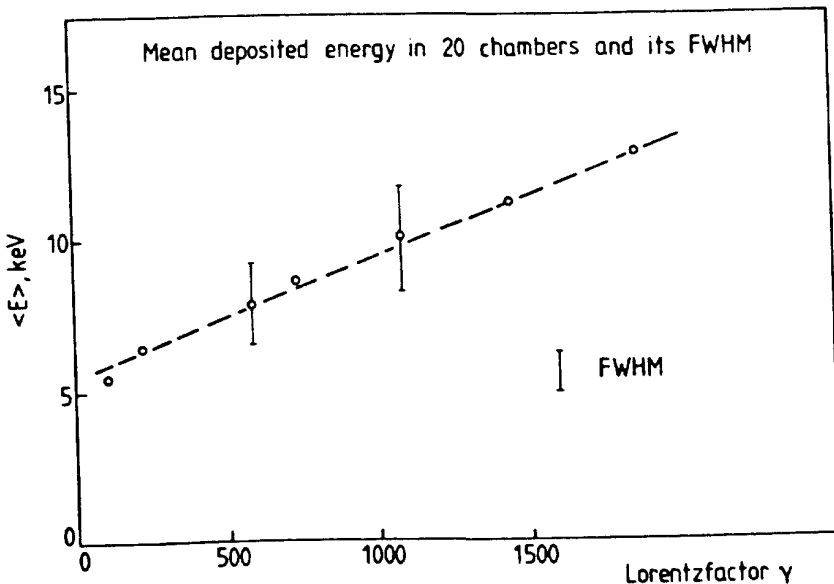


Fig.5. The observed dependence of a Transition Radiation detector signal on  $\gamma$ .

signals from the 20 stack EHS device (Commichau 1980, Struczinski 1983). In considering the probability of different masses at known momentum such phenomenological data are used rather than theoretical calculations.

### III.3 dE/dx detectors

#### III.3.1 Theoretical spectra and their velocity dependence

The cross sections described by equation (6) are large. For instance a relativistic particle passing through argon at atmospheric pressure makes a collision about every 300  $\mu\text{m}$ . It is not possible to measure the differential cross-section directly on a collision-by-collision basis and deduce a value for the velocity. Instead, practical detectors measure the energy (or ionisation) deposited in a fixed path length  $\ell$  in the gas more than a hundred times for each track Alikhanov (1956). The resulting energy-loss spectrum may be analysed to achieve the required resolution in  $\beta\gamma$ . In the following we show how to calculate the spectra and the resolution theoretically, how to analyse experimental spectra in practice and show examples of the velocity resolution that has been achieved in this way.

To calculate the spectrum of energy loss in a thickness  $\ell$  of gas we sum over the collisions occurring by the convolution method as follows:

- (1) Calculate the number of collisions,  $n = N \ell / \int \frac{d\sigma}{dE} dE$ .
- (2) Find  $v$ , the number of times  $\ell$  must be subdivided by 2 to reach a pathlength  $x$  in which the chance of a collision  $\tau$  is less than 10% - and therefore the chance of two or more collisions much less than 1%.
- (3) The energy-loss distribution in pathlength  $x$  is
$$F_x(E) = (1-\tau) \delta(E) + Nx \frac{d\sigma}{dE} + O(\tau^2)$$
- (4) The energy-loss distribution in pathlength  $2x$  is then

$$F_{2x}(E) = \int_0^E F_x(E-\Delta) F_x(\Delta) d\Delta$$

By  $v$  applications of this formula, the desired spectrum,  $F_\ell(E)$ , may be derived. In comparing such spectra with ionisation measurements we assume that ionisation is directly proportional to energy loss. Although untenable in detail this assumption is consistent with

available data and perfectly adequate for a discussion of  $dE/dx$  detectors.

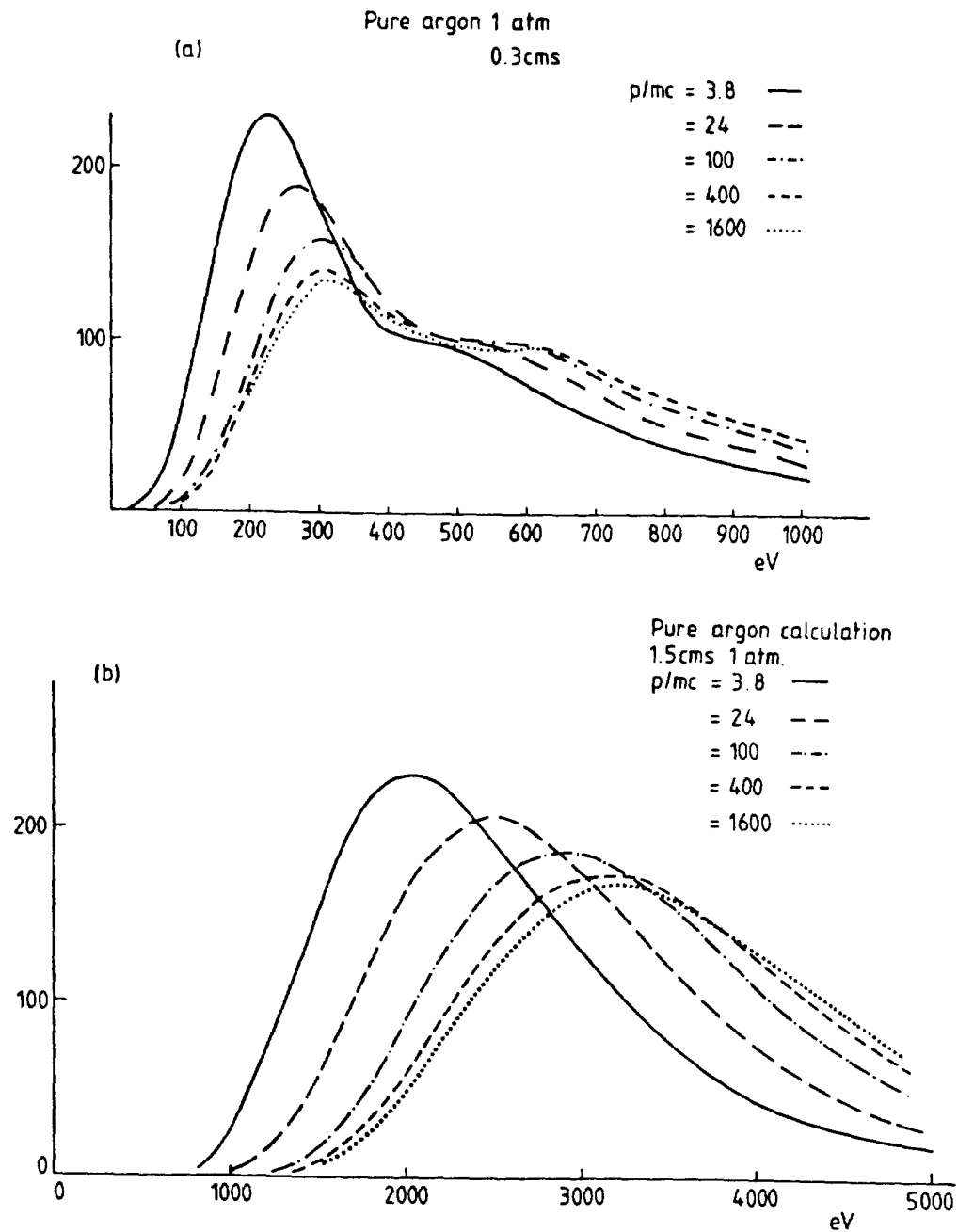


Fig.6. The calculated  $\beta\gamma$ -dependence of  $dE/dx$  spectra for a) 3 mmms and b) 5 mmms of argon.

Fig.6a shows  $dE/dx$  distributions for  $\approx 3$  mmms of pure argon at normal density calculated for different values of  $\beta\gamma$ . The changing shape arises from the vestigial effect of the shell structure. Fig.6b is a similar plot for  $\approx 15$  mmms of pure argon. Here the shape of the

distribution has become smooth and may be matched for different values of  $\beta\gamma$  by scale changes along the axes. The extent to which this is true is illustrated in fig.7 where the reduced width is plotted for different  $\beta\gamma$ . There is a small variation in width arising from the improved statistics when the ionisation is higher. We ignore this and assume that for  $\lambda$  fixed the distribution has a fixed universal shape  $F$  independent of  $\beta\gamma$ . A likelihood study shows that the resulting loss of information is small provided that the length  $\lambda$  is large enough (>1cm atm for argon).

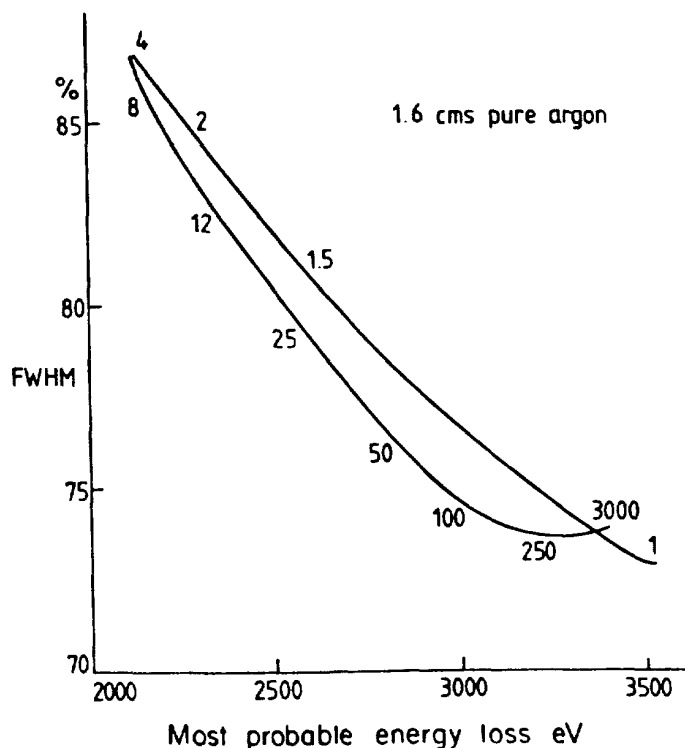


Fig.7. The calculated relative width of the energy-loss distribution as a function of the most probable energy-loss for 1.6 cms of pure argon at normal density. The numbers on the graph are the corresponding values of  $\beta\gamma$ .

### III.3.2 Determining velocity from experimental measurements

The most efficient fitting method with these assumptions is a single parameter likelihood method which maximises

$$L(\lambda) = \prod_i F(E_i/\lambda)$$

where the measurements  $E_i$  are scaled by the parameter  $\lambda$ .  $\lambda$  is proportional to the ionisation of the track. Fig.8 shows a comparison

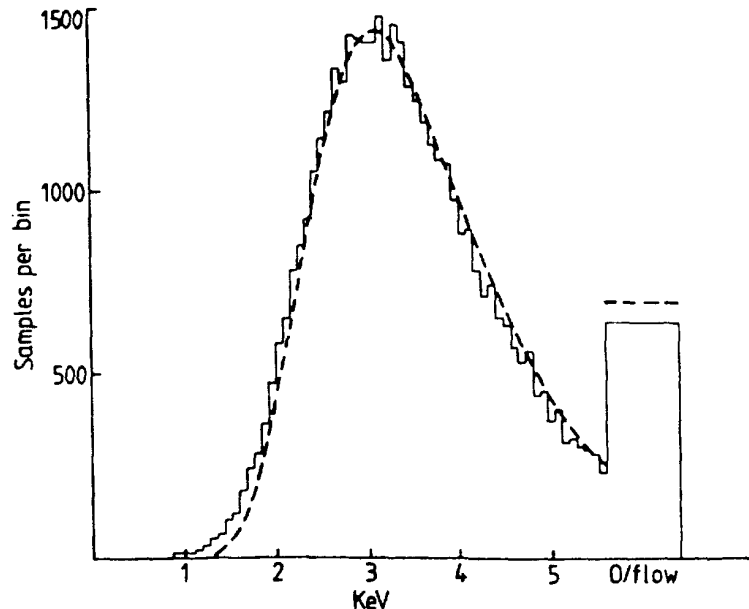


Fig.8. A comparison of theoretical and experimental  $dE/dx$  distributions. The experimental energy calibration is a free parameter.

of the theoretical distribution  $F$  for 1.6 cms of argon/20%  $\text{CO}_2$  at 1 atm with experimental data from ISIS2 on a large number of tracks (Allison 1974, 1982). The agreement is surprisingly good considering that instrumental effects such as resolution, crosstalk and diffusion have been ignored. With this level of agreement it is immaterial whether the theoretical or experimental distribution is used as likelihood function although in principle the latter is preferred. The advantages of the maximum likelihood method over the truncated mean method described below are threefold:

- (1) It provides not only a value of  $\lambda$  but an internal error.
- (2) It has a much superior dynamic range, providing unbiased estimates of  $\lambda$  even when 95% of the spectrum is in the 'overflow bin'.
- (3) It is unambiguous<sup>†</sup>.

Nevertheless in most cases it does not give a significantly superior ionisation resolution.

Fig.9 shows a theoretical analysis of the ionisation resolution,  $\Delta\lambda/\lambda$

---

<sup>†</sup> Some other methods involve technical ambiguities. For example, how do you calculate the unbiased mean of the lowest 40% of 99 measurements?

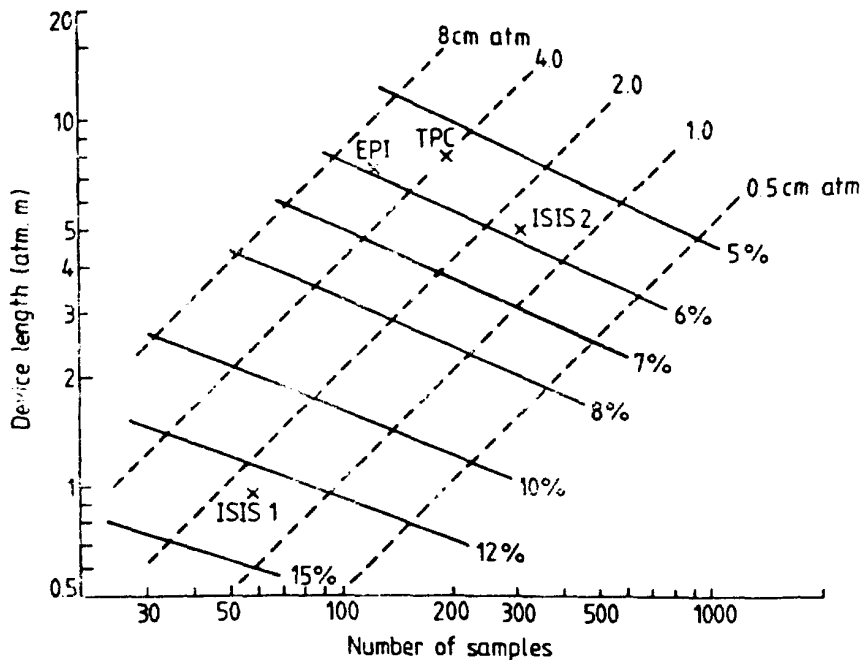


Fig.9. Calculated ionisation resolution (% FWHM) contours for argon with  $\beta\gamma=100$ . The crosses indicate the sizes and samplings of a number of devices. The dashed lines are loci of constant sample thickness.

(FWHM), that can be achieved with argon, as a function of the number of samples and the device length. The calculation uses the distribution for  $\beta\gamma=100$ . For thicknesses less than  $1\text{cm atm}^{\dagger}$  the shape of the distribution changes significantly with  $\beta\gamma$  as we have seen and the single parameter likelihood analysis described here is not optimal. Cruder methods of analysis such as the use of the mean of the lowest 50% of the signals (Lehraus 1978) yield similar values for the resolution in general but are significantly worse below  $1\text{cm atm}$  because they ignore the information in the shape of the spectrum. However this is rather academic for practical detectors because there are significant effects which make it very difficult to measure such thin samples independently on the scale needed (Lapique & Piuz 1980). For good separation of  $\pi/K$ /proton masses a FWHM resolution of order 6% is needed (2.5% RMS).

The calculated dependence of the ionisation on  $\beta\gamma$  for argon (Allison & Cobb 1980) is compared with experiment (Lehraus 1978) in fig.10. The

---

<sup>†</sup> To a first approximation the resolution depends only on the thickness in  $\text{gm cm}^{-2}$ . For gases this is conveniently measured as the product of path length times pressure where normal temperature is understood.

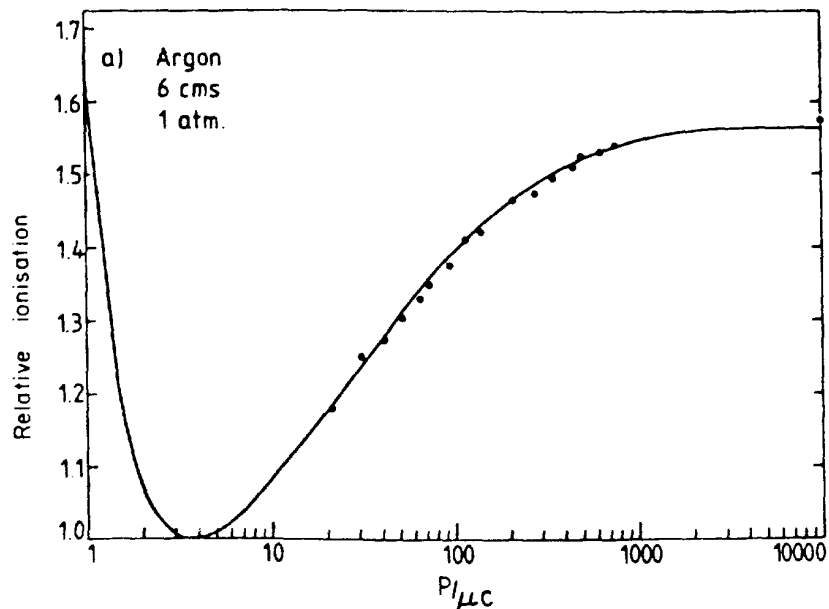


Fig.10. A comparison of the measurements of Lehraus 1978 with the calculated dependence of ionisation  $I/I_0$  on  $\beta\gamma = P/\mu c$ .

agreement is good. Calculations for a number of other gases, pressures and sample thicknesses have been published (Allison 1982). The dependence on choice of gas and sampling geometry favours fine sampling and the use of argon or possibly xenon. Fine sampling (down to 1cm atm) not only improves the resolution but even increases the relativistic rise a little.

### III.3.3 The calibration problem

In practice the main problem is one of calibration. The likelihood fit yields a value of  $\lambda$  for each track from its many ionisation measurements. The relationship between  $\lambda$  and the ionisation relative to minimum,  $I/I_0$ , involves:

- Track inclination ( $\theta$ ). For angles up to about  $45^\circ$   $\lambda$  is proportional to  $\sec\theta$  and may therefore be corrected by multiplying by  $\cos\theta$ .
- Amplification variation - possibly depending on the position in the detector.

Calibration may be attempted using signals from X-ray or other sources. This is often not easy. Instead here we describe a method that uses the tracks themselves assuming that a majority are pions. It proceeds in

two steps:

- a) Assume that all tracks are pions ignoring tracks that may be non relativistic. Calculate for each track the calibration factor  $G$  equal to the ionisation expected for a pion of the known track momentum divided by the corresponding value of  $\lambda \cos\theta$ . The first estimate of the calibration factor uses the mean value of  $G$ . This calibration is wrong but only by a few percent because in general only a small fraction of tracks are not pions and their ionisation differs by not more than 10-15% from that of a pion.
- b) Find those tracks whose momenta and ionisation errors are such that the expected ionisation for a pion is more than 4 standard deviations (say) from the electron or kaon hypothesis. Use the calibration from (a) on these to eliminate those tracks whose measured ionisation is more than 2.5 standard deviations from the pion expectation. Calculate a better value for the calibration factor by evaluating the mean  $G$  for the remaining tracks. This step may be iterated again although this brings little change.

Given the calibration and, for each track, the value of  $\lambda$  and its error, we may derive an experimental value of  $I/I_0$ . Knowing the track momentum this is compared with the expected value of  $I/I_0$  for each mass assignment using the known  $\beta\gamma$  dependence for the gas, for example fig.10. Monte Carlo simulation studies show that it is the logarithm of  $I/I_0$  that is normally distributed rather than  $I/I_0$  itself. We therefore calculate a  $\chi^2$  with 1 degree of freedom for each of the masses e,  $\pi$ , K and p:

$$\chi_M^2 = \frac{(z_M^{\text{th}} - z^{\text{exp}})^2}{(\Delta z)^2}$$

where  $Z$  is  $\ln(I/I_0)$ . This is the ionisation  $\chi^2$  for mass M.

#### III.3.4 Example of performance that can be achieved

In the case of the data from ISIS2 (Allison 1974, 1982) in the NA27 EHS experiment at the CERN SPS this method of calibration was checked by looking at electron candidates identified by a lead-glass wall (Aguilar-Benitez 1983). From a sample of about  $2 \times 10^4$  secondaries those that deposited between 0.8 and 1.3 times their energy (as measured by

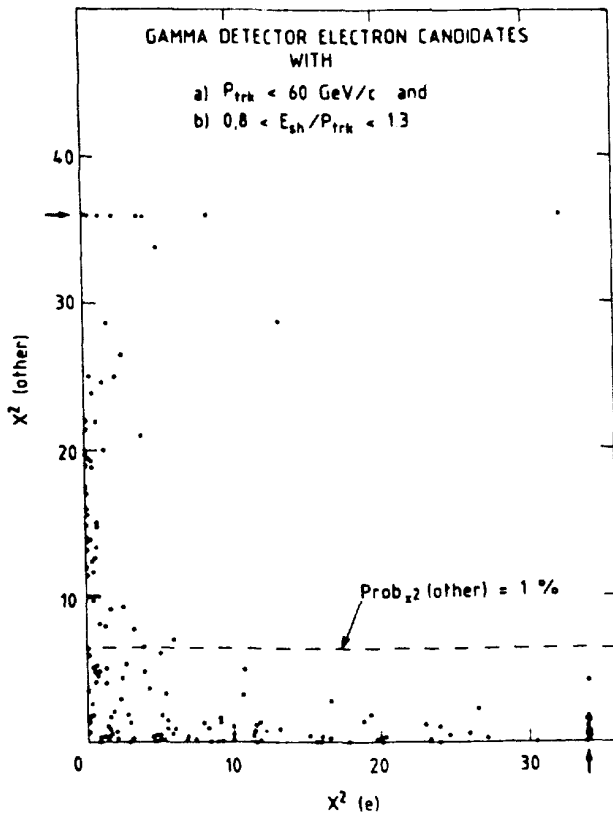


Fig.11. A scatter plot of ionisation chi-squares for electron candidates selected by the lead-glass wall. Values of  $\chi^2$  greater than 35 or so are shown superposed in line with the arrows.

magnetic dispersion) in the lead-glass were chosen. Fig.11 shows for these tracks a plot of the  $\chi^2$  for the electron hypothesis against the  $\chi^2$  for the best hadron hypothesis. The tracks divide almost equally into three categories; those in the corner that are compatible at the 1% level with either an electron or hadron interpretation; a horizontal band of those that are consistent with a hadron interpretation but incompatible with an electron (the fraction of these at a few  $\times 10^{-3}$  is consistent with the efficiency of the lead-glass detector); and a vertical band of confirmed electrons inconsistent with hadrons. Fig.12 shows the  $\chi^2$  probability distribution for the electron mass for all tracks with hadron probability less than 1%. The flat distribution confirms that the error used, which was  $106/\sqrt{N} \text{ % FWHM}$  where  $N$  is the number of samples, is correct. This is in complete agreement with the prediction shown in fig.9. The mean value of  $N$  in practice was 240 out of the maximum of 320 samples per track. The loss of samples is due mostly to track overlap (see appendix). The two tracks shown cross

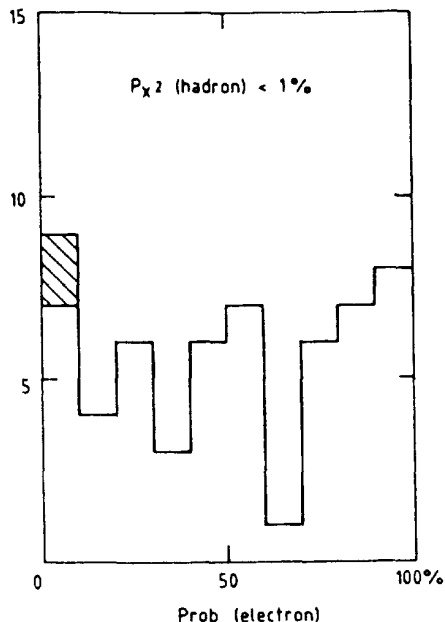


Fig.12. The ionisation probability distribution for those electron candidates whose ionisation is not compatible with any hadron.

hatched in fig.12 have ionisations incompatible with any mass. They represent a measure of current residual effects in the analysis.

Fig.13 is a scatter plot of  $I/I_0$  versus log momentum for several thousand secondaries in the NA27 charm experiment. The  $\pm 3\%$  bands expected for  $e$ ,  $\pi$ ,  $K$  and proton masses are shown. The plot shows separation according to the Rayleigh Criterion (1 FWHM or  $2.36\sigma$ ) for the following momentum ranges:

Mass pair	Momentum range (N=300)
$e, \pi$	Up to 25 GeV/c
$\pi, K$	2-60 GeV/c
$K, p$	5-40 GeV/c
$\pi, p$	1.5-150 GeV/c

Practical questions of separation depend on the confidence level sought and the relative fluxes concerned.

As a live example of  $dE/dx$  data we show in fig.14 the track hit data from ISIS2 for an event with a  $D^0$  decay uniquely identified by kinematics. Four charged tracks coming from the resolved  $D^0$  decay vertex in the bubble chamber are marked. The tracks shown are up to 5.12m long (horizontal axis) divided into 320 samples. The vertical

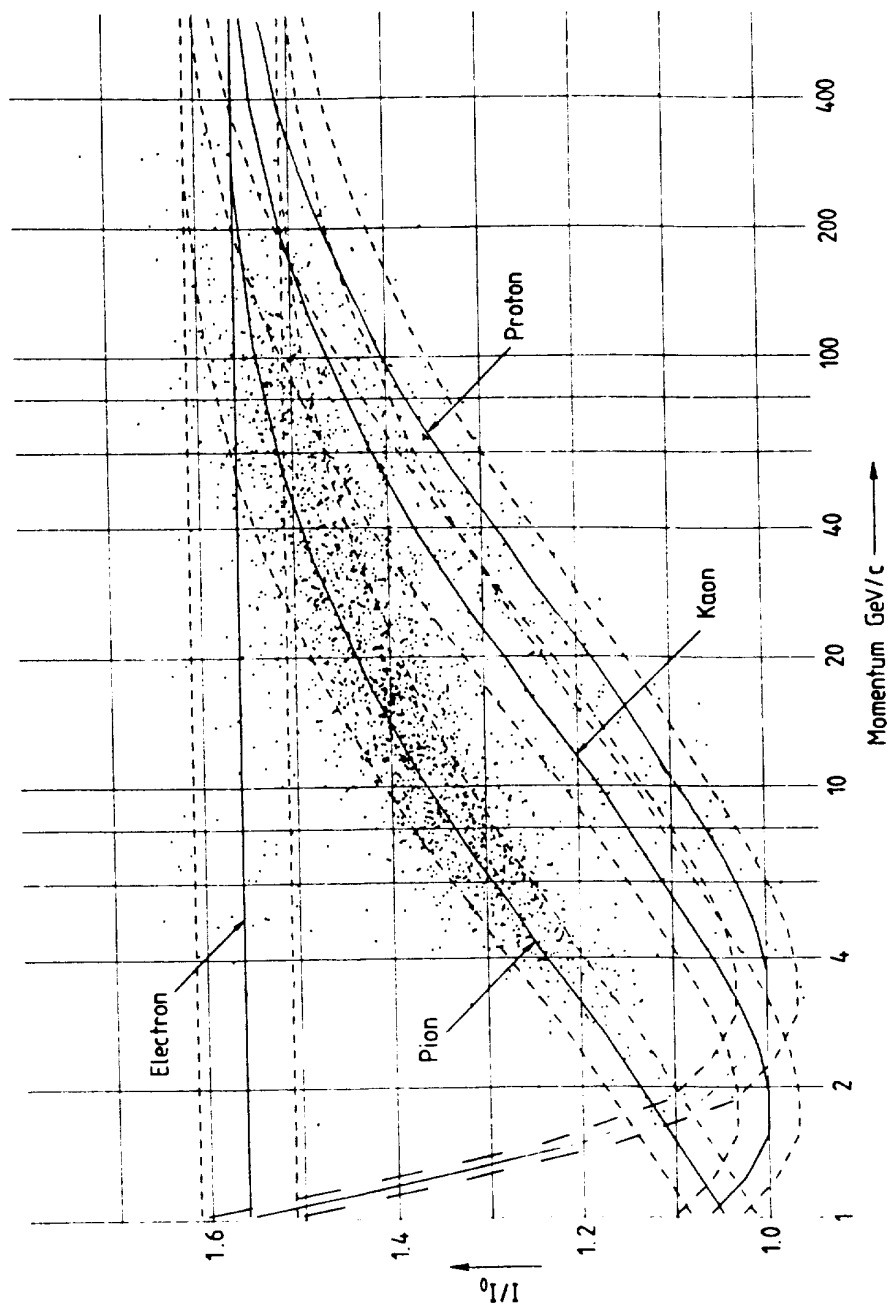


Fig.13. A scatter plot of measured values of ionisation  $I/I_0$  versus log momentum. The bands shown for  $\pi$ ,  $K$  and proton are discussed in the text.

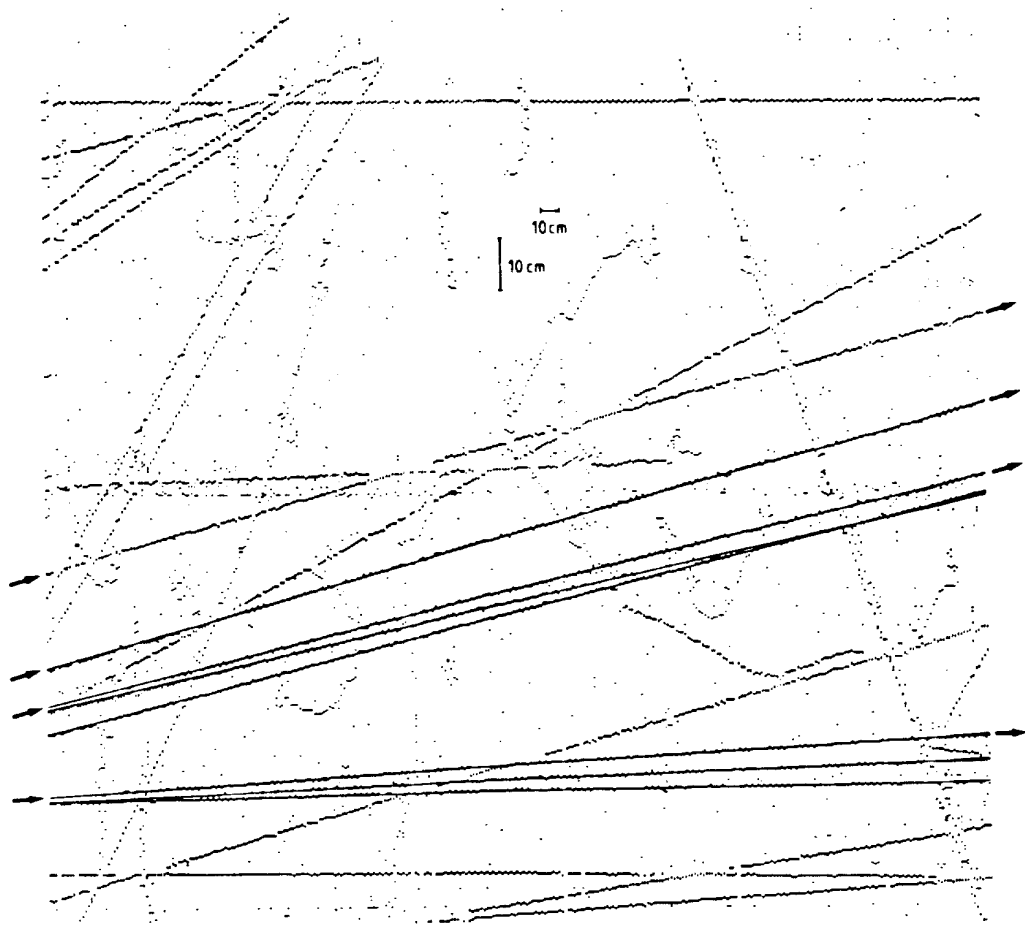


Fig.14. The track-hit data in ISIS2 for a single event which includes a reconstructed  $D^0$ . The four charged tracks from its decay are marked by arrows.

axis corresponds to 4m (folded). For each individual hit shown there is a 7-bit pulse height. The pulse heights associated with each track are histogrammed and fitted as described earlier. Fig.15 shows the data and fits for three of the tracks from the  $D^0$  decay. The tracks are clearly distinguished as  $K$  or  $\pi$  and this identification is confirmed in the unique kinematic fit based on momentum information alone. The situation is summarised in the table. The identification of the fourth track as a pion is poor but not ruled out.

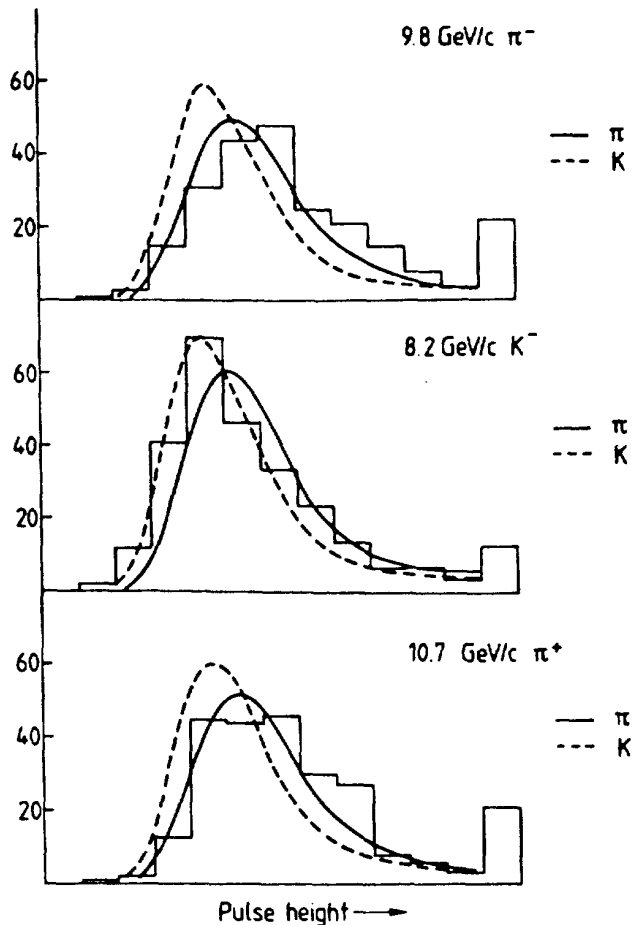


Fig.15. The  $dE/dx$  spectra of three of the charged tracks marked in fig.14. The superposed curves are the  $K$  and  $\pi$  predictions using the measured track momenta.

Track	Momentum GeV/c	# of samples	Ionisation $\pm$ RMS	Probability(%)			
				e	$\pi$	K	p
1	9.8 $\pi$	237	1.434 $\pm$ 3.0%	.5	5.4	<0.1	<0.1
2	8.2K	275	1.139 $\pm$ 2.8%	<0.1	<0.1	70.6	1.9
3	10.7 $\pi$	246	1.397 $\pm$ 2.9%	<0.1	42.5	<0.1	<0.1
4	5.1 $\pi$	247	1.156 $\pm$ 2.7%	<0.1	0.2	4.2	<0.1

Reference to experience with other detectors may be found in Lehraus (1983).

Appendix: The solution of practical problems for dE/dx detectors

The description of relativistic particle identification by  $dE/dx$  given in III.3 presupposes the solution of a number of problems. These are discussed here with the solutions adopted for the ISIS detector (Allison 1974, Aguilar Benitez 1983, Allison 1982) but the points are common to any large drift chamber seeking the necessary control of systematic effects (Pleming 1977). ISIS is a pictorial drift chamber whose prime role is particle identification; tracking is a free but impressive by-product. Fig.16 shows a vertical beam-plane section of the upstream part of the chamber. Track signals drift to a single central wire plane perpendicular to the plane of the diagram. The multihit electronics can handle between 30 and 50 hits per event on each wire and have been described elsewhere (Brooks 1978). The data include the drift time and pulse height for each hit. The third coordinate

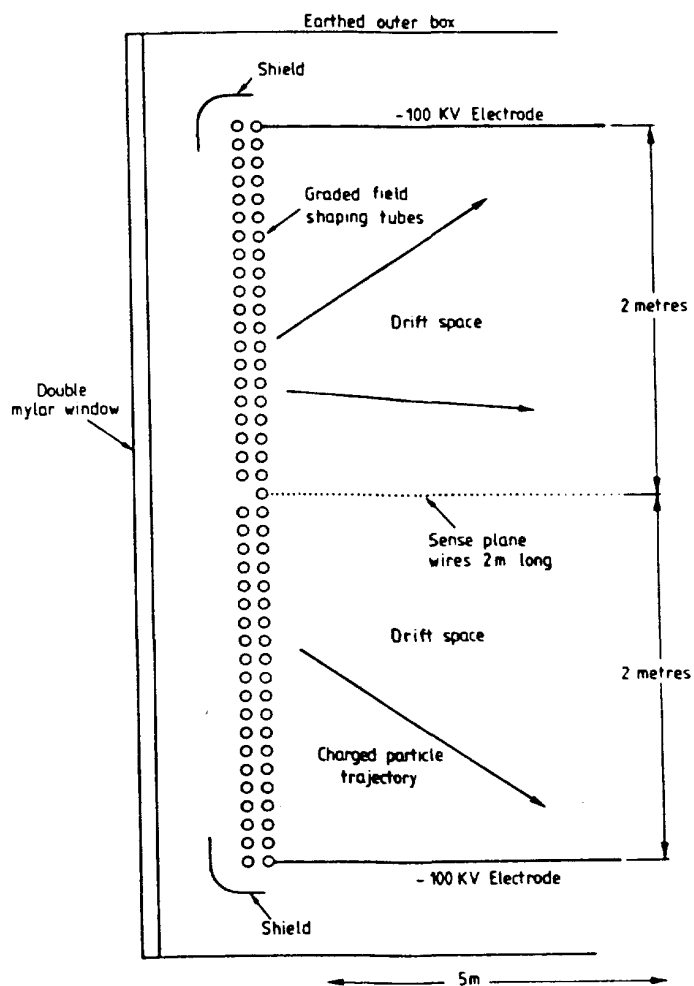


Fig.16. A diagram of ISIS2.

is not measured and the up-down ambiguity is not resolved by the chamber alone.

	<u>ISIS2</u>
Acceptance	$4 \times 2\text{m}^2$
Drift distance	$2 \times 2\text{m}$
Voltage	100 KV
Maximum number of Samples	320
Volume	$120\text{m}^3$
Ionisation resolution, FWHM (with 320 samples)	6.0%

### Factors affecting the achievement of uniform track-signal response

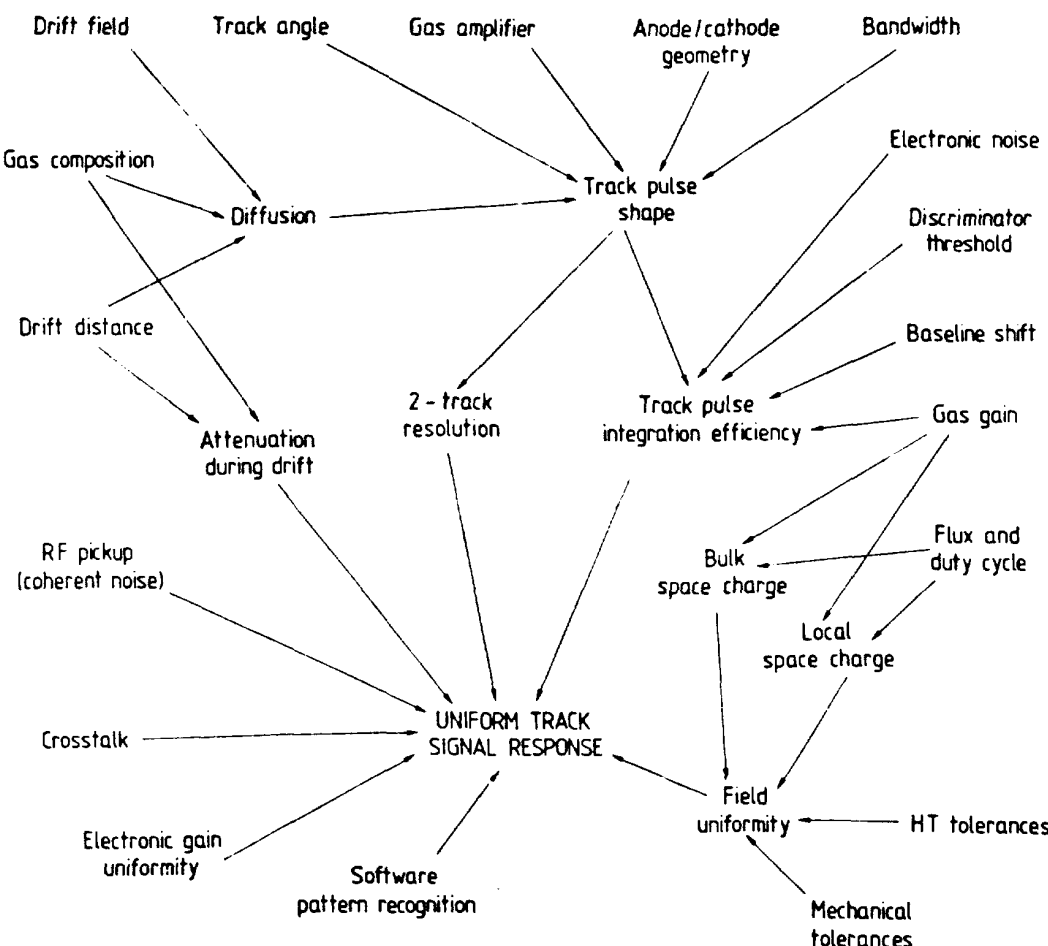


Fig.17

Fig.17 summarises the various relationships that determine the

uniformity of track signal response which needs to be free of systematic effects at the 1% level. The diagram indicates the important role of the shape of the track signals. An individual electron arriving at an anode wire and generating an avalanche produces a pulse with a long tail of the form  $1/t+t_0$  (Charpak 1970). This may be seen as the linear impulse response of the gas amplifier. Inverting to provide a short clipped pulse without undershoot is a linear problem. In ISIS it is done by a passive filter with three time constants - two is probably enough. Of course such correction need not reproduce a  $\delta$ -function. It is sufficient to match the pulse to the bandwidth of the electronics which in turn must be chosen to integrate the signal sufficiently. A relativistic particle makes about 30 collisions and 100 secondary electrons in 1 cm atm of argon. Depending on the track angle, diffusion and collection geometry these 100 electrons will be spread up to 1 cm in drift distance. With a drift velocity of  $2\text{cm}/\mu\text{s}$  (or  $20\mu\text{m}/\text{ns}$ ) the mean time between electron arrival is 5ns. In ISIS the bandwidth of the electronics is 15 MHz. This implies a typical instantaneous signal charge of about  $5-10 \times G$  electrons referred to preamplifier input where  $G$  is the gas amplification factor ( $10^4$  in ISIS). In terms of current this represents a typical peak 300-1000 namps with an rms noise of 18 namps. The detailed effect of electronic noise and electron arrival time was studied in a Monte Carlo program to demonstrate that the signal-to-noise ratio is sufficient to trigger efficiently (>99%) on tracks and rarely on noise ( $< 1 \text{ KHz}$ ). The collection geometry contribution to the track pulse shape comes from the variation of drift time for different drift paths near the anode wire. The effect of diffusion is important but may be minimised by using a suitable molecular "cooling" gas such as  $\text{CO}_2$  which keeps the r.m.s. energy of the electrons near to  $kT_e \sim 1/40 \text{ eV}$  (Allison 1974). An electron that drifts a distance  $l$  through a potential  $V$  has an r.m.s. displacement  $\sigma$  in each orthogonal dimension given by

$$\sigma/l = \sqrt{kT_e/\text{eV}}$$

where  $T_e$  is the electron temperature (assumed isotropic). Minimising  $\sigma$  has two other consequences. First, because the electrons are kept in thermal equilibrium with the gas as far as possible, it follows from kinetic theory that the drift velocity is not "saturated". This is in fact not seen as a disadvantage for the drift velocity is kept uniform by designing an electric field with the necessary uniformity ( $10^{-3}$ )

which is needed anyway if the necessary gain uniformity is to be achieved ( $10^{-2}$ ). The second consequence of the cooling gas is an increased sensitivity to residual oxygen concentration. The cooling gas catalyses the attachment of electrons to oxygen. Typically oxygen concentrations below 0.2 parts per million (by volume) must be achieved if loss by attachment is to be ignored (Allison 1974). Of course the exponential loss of pulse height with drift distance can be corrected if the loss is known. Calibrating this loss may mask other effects including imperfect track pulse integration efficiency.

The pulses have a variable shape as the effect of angle and diffusion varies from track to track. To measure the charge in a pulse it is therefore necessary to do a true gated integration of a slightly delayed track pulse with the front and back edge of the gate operated by a discriminator looking at the prompt track signal. The effects of electronic noise and modest gas amplification require the discriminator to have a finite threshold. Delays are incorporated in the logic to avoid missing part of the track signal due to the consequent slewing. A more insidious problem is the baseline shift at high rates. It is usual for the electronics to employ ac coupled signals to avoid the hazards of dc amplification. It follows that the mean signal amplitude is zero. In particular if the signal occupancy is  $f\%$  within one ac coupling time constant, the baseline will shift by  $f\%$  of the pulse height as shown in fig.18. Since the occupancy in ISIS for an event is 10% or more this is

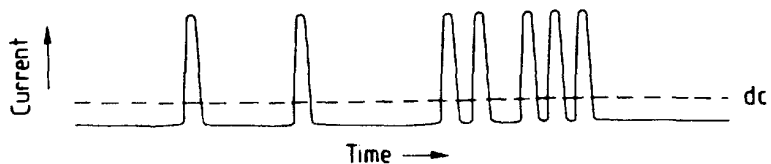


Fig.18. A pulse train illustrating the effect of ac coupling in creating a dc level shift.

a serious effect. It cannot be computed in practice from the amplitude of earlier pulses partly because of uncertainties surrounding the frequent saturating signals. The problem is essentially nonlinear and cannot be corrected with passive filters. There are two solutions - either the background level between pulses can be digitised and used for off-line correction, or the background level signal can be fed back in the electronics itself. In ISIS the latter was chosen. Once this

problem is solved excellent rejection of low frequency hum, or at least its linear consequences, can be achieved.

The need to reduce systematic biases to the 1% level leads to a very conservative two-track resolution. The values of the delays in the gated integration are designed to integrate 99% of the signal in the most unfavourable case as checked in the Monte Carlo simulation of the ISIS signal processing (Pleming 1977). The success of the optimisation may be judged from fig.19. The line superposed on the lower histogram is the expectation of Poisson statistics. All track hits separated by more than 15mms are resolved. The mean pulse-heights for the first and second hits of such pairs show that resolved hits above 15mms are unaffected by the presence of the other at the level of 2-3%.

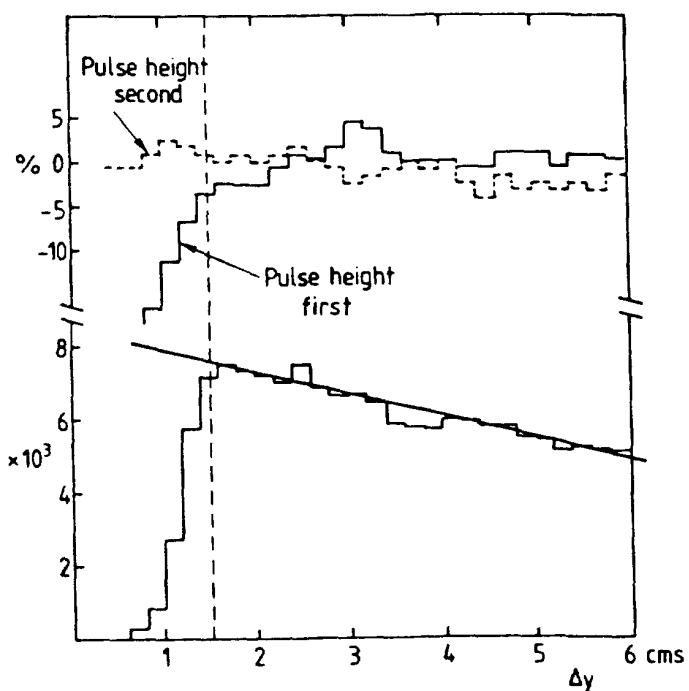


Fig.19. Lower histogram - the distribution of resolved track hits as a function of track separation. Upper plot - the dependence of mean pulse height on track separation.

To achieve uniform track-signal response it is also necessary to have stable uniform gas amplification. This depends on the uniformity of the gas composition, the charge per unit length of the anode wire and its diameter. Since the gas amplification is an avalanche process involving 10 or more generations the uniformity required to achieve 1% gain stability is about 0.1%. (The measured dependence of gain on small

variations of gas pressure, for example, shows a factor of 7). Since the voltage difference between the anode wire and all other conductors may be controlled relatively easily the problem is to control the dimensions such that the capacitance is sufficiently uniform. With careful design these problems can be solved. More difficult are the effects of space charge on the anode wire charge. These separate into two parts, bulk space charge and local space charge. Bulk (drift volume) space charge. As a result of cosmic rays, background and earlier events the drift volume always contains positive ions released during the gas amplification process. One can estimate roughly the density  $\rho$  knowing the gas amplification factor  $G$ , the mean ionisation rate ( $100e/cm$ ) and the positive ion drift velocity ( $\sim 1cm/s/volt/cm$ ). Bulk space charge will be a problem for both spatial precision (at  $10^{-3}$  level) and gain uniformity (at  $10^{-2}$  level) if

$$\frac{\int \rho(z) dz}{\sigma} > 10^{-3}$$

The integral is the line integral of the space charge density through the drift volume and  $\sigma$  is drift electrode charge density per unit area. We have reported spectacular effects from such space charge. In ISIS we have cured the problem by gating the gas amplification off except during the bubble chamber sensitive time. The problem is a major constraint for any detector of this type. ISIS has no such effect with the following parameters:

Amplified flux (total)	1200 tracks/second
Drift field	$5 \times 10^4$ Volts/metre
Pressure	1 atmosphere
Gas gain	$10^4$
Drift distance	2 metres

The second space charge effect is local space charge in the immediate neighbourhood of the anode. Fig.20 shows a track crossing a series of anode wires at an angle  $\theta$ . The avalanche for this track (ignoring diffusion) takes place over a length of wire  $s\theta$  where  $s$  is the anode separation. This size of the avalanche is of order

$$G(\text{gain}) \times P(\text{bar}) \times 10(\text{electrons/mm}) \times s(\text{mm}) \times 1.6 \times 10^{-19}$$

giving a linear density of avalanche

$$GP\theta^{-1} \times 1.6 \times 10^{-18} \text{ Coulombs/mm.}$$

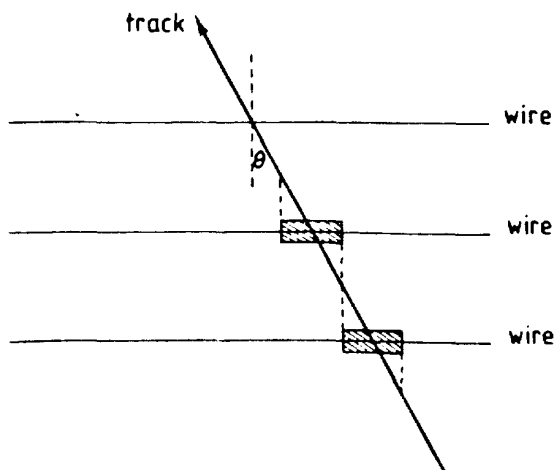


Fig.20. Where the gas avalanche occurs along the anode wires for a track at angle  $\theta$ .

If this charge density is significant (at level  $10^{-3}$ ) compared with the anode charge density causing the avalanche, the gain will be non linear. This is the so called "semiproportional" region of gas amplification but its singular dependence on angle is quite unsatisfactory. The charge density on a  $25\mu\text{m}$  anode wire is typically  $12\text{pC/mm}$ . In practice we observe no effect if  $GP\theta^{-1}$  is less than  $2\times 10^5$ . Tracks at angles less than 50 mrad in ISIS are avoided by rotating the chamber such that all tracks have significant values of  $\theta$ . Detailed observations by Frehse (1978) confirm back-of-envelope estimates although diffusion during the drift helps to spread the avalanche out. However there is another effect that makes matters worse. Since the positive ions travel very slowly (5-10 m/s), any track that arrives within a msec on the same section of wire as an earlier track will suffer from the influence of the earlier ions which are still only a few mms from the anode. In ISIS such an effect is observed (15% gain reduction) when the beam is finely focussed (instantaneous rate of order  $2.5\times 10^4$  tracks per sec per cm). There is no such effect with a defocussed beam.

Monitoring changes in the gas density and composition is a task that must be taken seriously. Temperature variations of a fraction of a degree or a millibar pressure change must be recorded. Thermal conductivity devices are good for monitoring binary gas mixtures, but measuring the oxygen contamination is harder. This is done with commercially available instruments based either on an aqueous alkaline electrolyte or a solid zirconia electrolyte. The trouble is that the

former do not work with  $\text{CO}_2$  and the latter run at high temperature. However available instruments have improved dramatically in the last few years.

Radio frequency pickup must be avoided. With very long anodes and sensitive low-noise electronics the problem demands careful design. A related problem is crosstalk of real signals between channels. This may have many causes of which capacitative crosstalk in the chamber or coupling through power supplies in the electronics are two. Another is diffusion. Because the  $dE/dx$  distribution is so highly skew the effect of diffusion crosstalk between nearest-neighbour samples causes the  $dE/dx$  peak not only to broaden but to shift to higher values with increasing drift distance. For a device that had either smaller samples or longer drift or was trying to get better resolution than ISIS2 this effect would become a problem. Diffusive crosstalk is positive while capacitative crosstalk is of negative sign. Generally Monte Carlo studies show that a few percent crosstalk between nearest neighbours is tolerable. Effects that couple all channels together are quite intolerable and lead to a dramatic loss in ionisation resolution.

To monitor the performance of the electronics *in situ* as well as keeping an eye on the software pattern recognition, two artificial "tracks" are included in every data readout. First there is a dummy track with a forced trigger whose pulse heights represent pedestal measurements (this is not plotted in the picture such as fig.14). Second there is a pulse generator signal sent to all channels in parallel and injected on the front of the preamplifier. This may be seen running across near the top in fig.14. Both the hardware and software treat this as any other track. Subsequently we find that this track has a pulse height resolution of <1% FWHM with individual measurements that have been successfully cleaned of overlapping signal regions. It is of course an important aspect of the design that in the main the same channels of electronics see every track so that problems of calibration between channels are of reduced importance. The detailed track filtering in the software is crucial. In fig.21 we show an expanded portion of fig.14. The hits are coded with different symbols depending on how they are used. The diamonds are the track hits used. The vertical bars are the track hits discarded as double on the grounds that they belong to two or more track vectors. The horizontal bars are

noise or  $\delta$ -ray hits. The long sloping lines are the track vectors from the overall fit in the spectrometer. One can see by inspection that the contamination by double track hits is less than 1%.

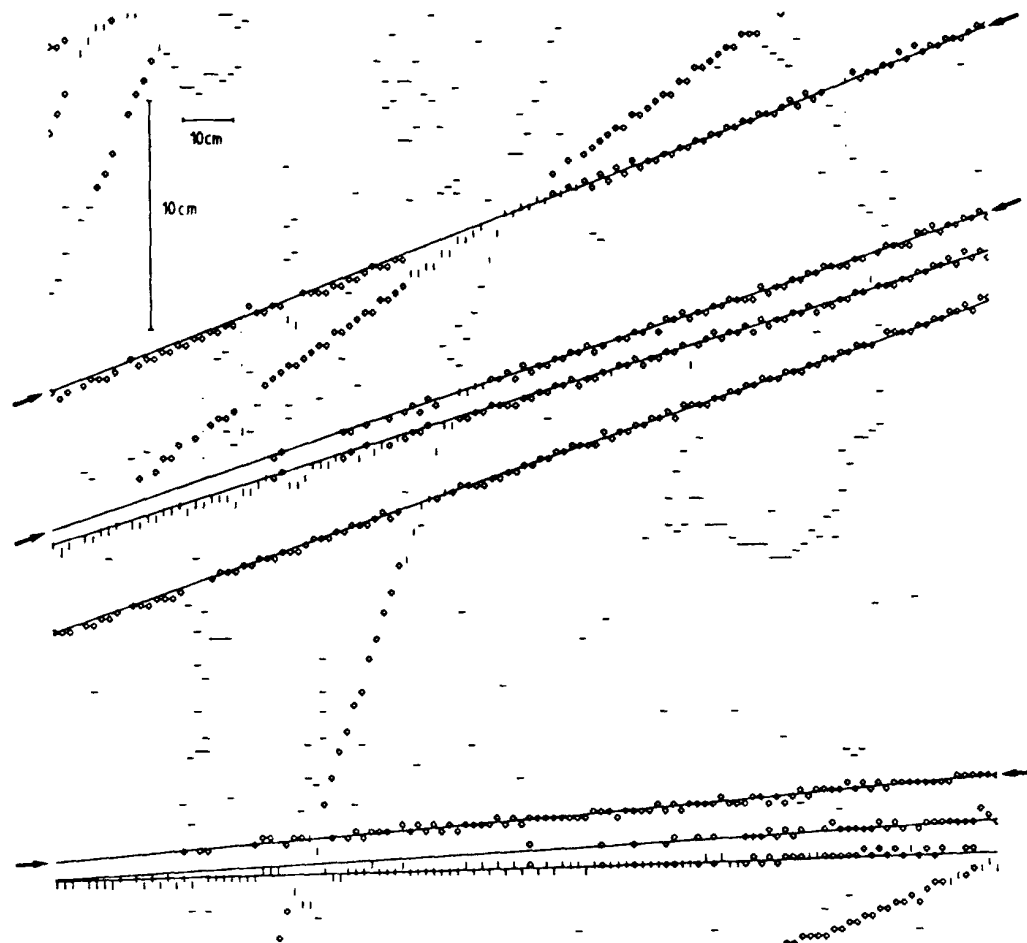


Fig.21. Detail of fig.14, 60 cms  $\times$  2 m long in space.

References

- Aguilar-Benitez (1983) Nucl. Inst.& Meth. 205, 79
- Alikhanov (1956) Proc. CERN Symp.on High Energy Accelerators, Pion Phys.2, 87
- Allison et al (1974) Nucl. Inst.& Meth. 119, 449
- Allison and Cobb (1980) Ann.Rev.Nucl.i-Sart.Sci. 30, 253
- Allison (1982) Conf.on Instrumentation, SLAC-250, 61
- Artru et al (1975) Phys.Rev. D12, 1289
- Bauche et al (1982) Conf.on Instrumentation, SLAC-250, 122
- Berkowitz (1979) "Photoabsorption, Photoionisation and Photoelectron Spectroscopy" Academic Press (New York)
- Brooks et al (1978) Nucl. Inst.& Meth. 156, 297
- Cerenkov (1958) in Nobel Lectures, Elsevier (1964), Amsterdam
- Charpak (1970) Ann.Rev.Nucl.Sci. 20, 195
- Cobb et al (1977) Nucl. Inst.& Meth. 140, 413
- Commichau et al (1980) Nucl. Inst.& Meth. 176, 325
- Davenport et al (1983) IEEE Trans.NS 30, 35
- Fabjan (1975) Phys.Letters 57B, 484
- Fabjan (1977) Nucl. Inst.& Meth. 146, 343
- Fano (1963) Ann.Rev.Nucl.Sci. 13, 1
- Frehse (1978) Nucl. Inst.& Meth. 156, 87
- Garibyan (1957) JETP 33, 1403 [Soviet Physics JETP 6, 1079 (1958)]
- Garibyan et al (1975) Nucl. Inst.& Meth. 125, 133
- Glass et al (1983) IEEE Trans.NS 30, 30
- Jackson (1962) "Classical Electrodynamics" (First edition) John Wiley, New York, §§14.9
- Jackson (1975) "Classical Electrodynamics" (Second edition) John Wiley, New York, §§13
- Jelley (1958) "Cerenkov Radiation" Pergamon (London)
- Ladron de Guevara (1983) EHS Internal note.
- Landau and Lifshitz (1960) "Electrodynamics of Continuous Media" Pergamon, Oxford §§85 & 86
- Lapique and Piuz (1980) Nucl. Inst.& Meth. 175, 297
- Lehraus et al (1978) Nucl. Inst.& Meth. 153 347
- Lehraus (1983) Proc.of Vienna Wire Chamber Conf., Nucl. Inst.& Meth.
- Litt and Meunier (1973) Ann.Rev.Nucl.Sci. 23, 1

- Pleming (1977) D.Phil.thesis, Univ.of Oxford, Rutherford HEP/T/69  
Poelz and Riethmuller (1982) Nucl.Inst.& Meth. 195, 491  
Struczinski (1983) Internal EHS note.  
Ter-Mikaelian (1972) "High Energy Electromagnetic Processes in Condensed Media" Wiley-Interscience (New York)  
Ypsilantis (1981) Physica Scripta 23, 371